

# Understanding Mn-modulated restructuring of Fe-based catalysts for controlling selectivity in CO<sub>2</sub> hydrogenation to olefins

Received: 24 June 2024

Accepted: 7 April 2025

Published online: 02 June 2025



Qingxin Yang<sup>1,4,5</sup>✉, Elizaveta A. Fedorova<sup>1,5</sup>, Dong-Bo Cao<sup>2,5</sup>, Erisa Saraçi<sup>3</sup>, Vita A. Kondratenko<sup>1</sup>, Carsten R. Kreyenschulte<sup>1</sup>, Henrik Lund<sup>1</sup>, Stephan Bartling<sup>1</sup>, Jana Weiß<sup>1</sup>, Dmitry E. Doronkin<sup>3</sup>, Jan-Dierk Grunwaldt<sup>3</sup>, Angelika Brückner<sup>1</sup>, Haijun Jiao<sup>1</sup> & Evgenii V. Kondratenko<sup>1</sup>✉

For CO<sub>2</sub> hydrogenation over iron-based catalysts, revealing the promoting effect of manganese and the nature of catalytically active sites remains a challenge that hinders targeted catalyst design. Here we elucidate the manganese-modulated restructuring of such catalysts during preconditioning and CO<sub>2</sub> hydrogenation using in situ X-ray absorption spectroscopy. The reaction-induced decoration of the surface of iron carbide with a MnO-containing layer is essential to hinder methane formation in favour of C<sub>2</sub>–C<sub>4</sub> olefins and C<sub>5+</sub> hydrocarbons. The selectivity changes were rationalized via spatially resolved steady-state and time-resolved (micro)kinetic tests combined with density functional theory calculations. The promoter affects the ability of iron carbide to generate surface species from H<sub>2</sub>, CO<sub>2</sub> and C<sub>2</sub>H<sub>4</sub>, thus controlling the surface C/H ratio, which is decisive for product selectivity. Consequently, the design of efficient multi-component heterogeneous catalysts requires a thorough understanding of the optimal catalyst architecture and, in particular, how to generate and stabilize it under reaction conditions.

Throughout the historical development of heterogeneous catalysts, the promotional effects of dopants have always been an attractive topic in both fundamental and industrial studies<sup>1,2</sup>. Promoters are considered to produce electronic and/or geometric effects on active sites/phases and consequently influence the interaction of reactants/intermediates/products with the catalyst, and its structural evolution under the reaction conditions<sup>3–5</sup>. Notable examples of large-scale applications include the alkali promotion of iron- or ruthenium-based catalysts in ammonia synthesis<sup>6,7</sup> and the ZnO promotion of copper-based catalysts in methanol synthesis<sup>8,9</sup>.

The promotion of Fe-based catalysts used for the direct hydrogenation of carbon dioxide (CO<sub>2</sub>) to lower olefins and fuels (known as CO<sub>2</sub>-based Fischer–Tropsch synthesis (CO<sub>2</sub>-FTS)) is also a hot topic of ongoing research<sup>10–12</sup>. This reaction provides a promising strategy, especially with the use of green hydrogen (H<sub>2</sub>), to decrease our reliance on fossil fuels and to close the carbon cycle. From a mechanistic viewpoint, CO<sub>2</sub> is initially converted to carbon monoxide (CO) followed by CO-based Fischer–Tropsch synthesis (CO-FTS) to produce higher (C<sub>2+</sub>) hydrocarbons<sup>13–16</sup>. Unpromoted Fe-based catalysts, however, have delivered poor selectivity for the desired products due to the

<sup>1</sup>Leibniz-Institut für Katalyse e.V., Rostock, Germany. <sup>2</sup>State Key Laboratory of Coal Conversion, Institute of Coal Chemistry, Chinese Academy of Sciences, Taiyuan, People's Republic of China. <sup>3</sup>Institute of Catalysis Research and Technology, Karlsruhe Institute of Technology, Eggenstein-Leopoldshafen, Germany. <sup>4</sup>Present address: State Key Laboratory of Heavy Oil Processing, China University of Petroleum (Beijing), Beijing, China. <sup>5</sup>These authors contributed equally: Qingxin Yang, Elizaveta A. Fedorova, Dong-Bo Cao. ✉e-mail: [qingxin.yang@cup.edu.cn](mailto:qingxin.yang@cup.edu.cn); [evgenii.kondratenko@catalysis.de](mailto:evgenii.kondratenko@catalysis.de)

high activity of CO/CO<sub>2</sub> methanation<sup>11,12</sup>. The use of promoters is one of the most efficient approaches for designing selective Fe-based catalysts<sup>17–22</sup>. Manganese, among others, has been introduced into Fe-based catalysts for CO<sub>2</sub>-FTS<sup>23–25</sup>, as inspired by the practice of optimizing catalyst formulations for CO-FTS<sup>26–31</sup>. Nevertheless, there have been many controversial reports on the function of this promoter. Its presence was concluded to lead to an increase in olefin selectivity<sup>23,32</sup>. On the contrary, other researchers have found that this promoter leads to a decrease in catalyst activity<sup>24</sup> and olefin production<sup>33</sup>. There have also been conflicting conclusions regarding the role of the Mn promoter in the formation of iron carbides (Fe<sub>x</sub>C<sub>y</sub>)<sup>26,30,34</sup>. The above discrepancies are partially due to the fact that Mn has typically been used as a co-promoter with an alkali metal<sup>18,24,35</sup>, with the latter being well-known to introduce additional complexity into the structure of the catalyst and the reaction mechanism.

It has also been recognized that heterogeneous catalysts tend to dynamically change their structure, for example, metal dispersion/sintering, component migration or phase transformation, upon interaction with the reactive atmosphere<sup>36–39</sup>. The mechanistic knowledge behind such reaction-induced catalyst restructuring, however, remains underexplored but is needed for targeted catalyst design. In this regard, Fe-based catalysts used in CO/CO<sub>2</sub>-FTS represent a notable but challenging platform; their transformations to Fe<sub>x</sub>C<sub>y</sub> compounds is decisive<sup>15,40,41</sup>. Therefore, an understanding of the catalyst dynamics under the reaction conditions and their influence on the catalyst performance are of fundamental importance and may provide new opportunities to unravel the mysteries of how multi-component catalysts function, especially at the atomic level, and to guide tailored catalyst design.

Motivated by the above challenges and opportunities, here we provide the fundamentals of the promoting effect of Mn for developing Fe-based catalysts with high selectivity for lower olefins and liquid fuels in CO<sub>2</sub>-FTS. The performance achieved in this study compares favourably with that of state-of-the-art alkali-free catalysts. The critical role of Mn species in modulating reduction- and reaction-induced catalyst restructuring was revealed using time-resolved in situ X-ray absorption spectroscopy (XAS). Advanced microscopy, electron energy-loss spectroscopy (EELS), microkinetic analysis using a temporal analysis of products (TAP) reactor and spatially resolved kinetic analysis of CO<sub>2</sub>-FTS, complemented by computational studies, were instrumental for understanding how the presence of Mn affects the ability of catalytically active Fe<sub>x</sub>C<sub>y</sub> to adsorb/activate CO<sub>2</sub>, H<sub>2</sub> and ethylene (C<sub>2</sub>H<sub>4</sub>) and to provide the fundamentals behind them.

## Results

### Platform of Fe–Mn catalysts and their characteristics

A series of Fe-based materials with different Mn/Fe atomic ratios (xFe–yMn; Supplementary Table 1) were synthesized via co-precipitation. α-Fe<sub>2</sub>O<sub>3</sub> (haematite) is the only crystalline phase present in the catalysts with Mn/Fe ratios ranging from 0 (for 10Fe–0Mn) to 0.11 (9Fe–1Mn) (Supplementary Fig. 1a). The fraction of this phase decreases as the Mn/Fe ratio increases due to the presence of X-ray amorphous phase(s), whereas the α-Fe<sub>2</sub>O<sub>3</sub> crystallite size does not change (13–15 nm; Supplementary Table 1). When the Mn/Fe ratio increases above 0.11 (9Fe–1Mn), Fe is predominantly present in X-ray amorphous phase(s), which dominate in the 7Fe–3Mn catalyst. The crystalline Mn<sub>3</sub>O<sub>4</sub> phase was identified in the 5Fe–5Mn catalyst (Supplementary Fig. 1a). The Mn-mediated decrease in the crystallinity of α-Fe<sub>2</sub>O<sub>3</sub> may cause the increase in the specific surface area from 37.6 m<sup>2</sup> g<sup>−1</sup> (for 10Fe–0Mn, the most crystalline material) to 235 m<sup>2</sup> g<sup>−1</sup> (for 7Fe–3Mn, the least crystalline material) and then the decrease to 182 m<sup>2</sup> g<sup>−1</sup> (for the 5Fe–5Mn, the second least crystalline material) (Supplementary Table 1).

The haematite characteristic bands in the Raman spectra of the catalysts become weaker and broader as the Mn content increases (Supplementary Fig. 1b). This result, together with the appearance of

the 1LO (first-order longitudinal optical) mode (at 660 cm<sup>−1</sup>), suggests a decrease in the haematite crystallinity due to the incorporation of Mn (Supplementary Note 1). The haematite amorphization was further proved via XAS at the Fe K edge (Supplementary Fig. 1c,d and Supplementary Note 2). Extended X-ray absorption fine-structure (EXAFS) analysis at the Mn K edge also indicates that Mn should be stabilized as a mixed amorphous Fe–Mn oxide in 7Fe–3Mn (Supplementary Fig. 2). The consequences of the above structural differences between the catalysts on the generation of steady-state phases under CO<sub>2</sub>-FTS conditions and their role in the formation of reaction products are discussed below.

### Catalytic performance in CO<sub>2</sub>-FTS

The 10Fe–0Mn catalyst changed its performance in CO<sub>2</sub>-FTS during the first ten hours on stream at 250 °C and then reached steady-state operation (Fig. 1a). All Mn-containing catalysts showed low CO<sub>2</sub> conversion ( $X(\text{CO}_2)$ ; <5%) at this temperature (Fig. 1b and Supplementary Fig. 3), probably due to a hindering effect of the promoter on the reverse water–gas shift (or RWGS) reaction that provides the CO needed for the in situ formation of Fe<sub>x</sub>C<sub>y</sub>.

When the reaction temperature was increased to 300 °C, the CO<sub>2</sub> conversion increased, too, but to a different extent depending on the Mn content. The higher the Mn content, the less pronounced the increase (Fig. 1a,b and Supplementary Fig. 3). For all Mn-containing catalysts, the change in conversion with time on stream was accompanied by a clear evolution in product selectivity. The selectivity for CO ( $S(\text{CO})$ ) declined, whereas the selectivity for C<sub>2+</sub> hydrocarbons ( $S(\text{C}_{2+})$ ) increased due to the contribution of CO-FTS. A steady-state operation was directly achieved over 10Fe–0Mn, 9.9Fe–0.1Mn and 9.5Fe–0.5Mn at 350 °C. The catalysts with a higher Mn loading (Mn/Fe ratio > 0.11) still needed about 50 h on stream to operate stably. Such Mn-dependent induction behaviour could be related to the different ability of the catalysts to form Fe<sub>x</sub>C<sub>y</sub> in situ, which is surely responsible for the formation of higher hydrocarbons.

The Fe-related integral rate of CO<sub>2</sub> consumption at a steady state (350 °C after 200 h on stream) initially increases with rising Mn content and reaches its highest value over the 9Fe–1Mn, 7Fe–3Mn and 5Fe–5Mn catalysts (Fig. 1c). The content of Mn is also important for olefin selectivity (Fig. 1c,d and Supplementary Fig. 4). As expected from previous studies<sup>24,42</sup>, the highest selectivity for methane ( $S(\text{CH}_4)$ ) was achieved over 10Fe–0Mn. It was decreased over the 9.9Fe–0.1Mn, 9.5Fe–0.5Mn and 9Fe–1Mn catalysts. Notably, the decrease in  $S(\text{CH}_4)$  was accompanied by an increase in the selectivity for C<sub>2</sub>–C<sub>4</sub> olefins ( $S(\text{C}_2^+=\text{C}_4^=)$ ) and C<sub>5+</sub> hydrocarbons ( $S(\text{C}_{5+})$ ). This conclusion is supported by the chain-growth probability  $\alpha$  (Fig. 1d and Supplementary Figs. 5 and 6). Both the highest  $\alpha$ -value and  $S(\text{C}_{5+})$  were determined over 9Fe–1Mn. The ratio of light olefins to light alkanes ( $O(\text{C}_2\text{--C}_4)/A(\text{C}_2\text{--C}_4)$ ) follows the same tendency (Fig. 1c). However, a further increase in the Mn loading led to a decrease in  $S(\text{C}_2^+=\text{C}_4^=)$  and  $O(\text{C}_2\text{--C}_4)/A(\text{C}_2\text{--C}_4)$  but to an increase in  $S(\text{CH}_4)$ .

In comparison with previously developed Fe-based catalysts promoted by a transition metal, including Mn, our best-performing 9Fe–1Mn catalyst showed a lower  $S(\text{CH}_4)$  at relatively high CO<sub>2</sub> conversion (Fig. 1e); it also showed better performance in terms of  $O(\text{C}_2\text{--C}_4)/A(\text{C}_2\text{--C}_4)$  (Fig. 1f). The achieved  $S(\text{C}_{2+})$  above 60% at 36% CO<sub>2</sub> conversion surpasses that reported for other catalysts (Fig. 1g). Survey X-ray photoelectron spectroscopy (XPS) scans of 9Fe–1Mn (Supplementary Fig. 7) excluded the presence of traces of any alkali metal, which is effective for lowering CH<sub>4</sub> formation in favour of desired hydrocarbons.

Although the presence of Mn in the catalysts resulted in an increase in the time that is required to achieve steady-state operation, suitable Mn contents lowered the selectivity for CH<sub>4</sub>, enhanced the production of lower olefins and facilitated the chain-growth reaction during CO<sub>2</sub>-FTS. The fundamentals behind the promoting effects of Mn are elucidated in the following sections, by considering the results of

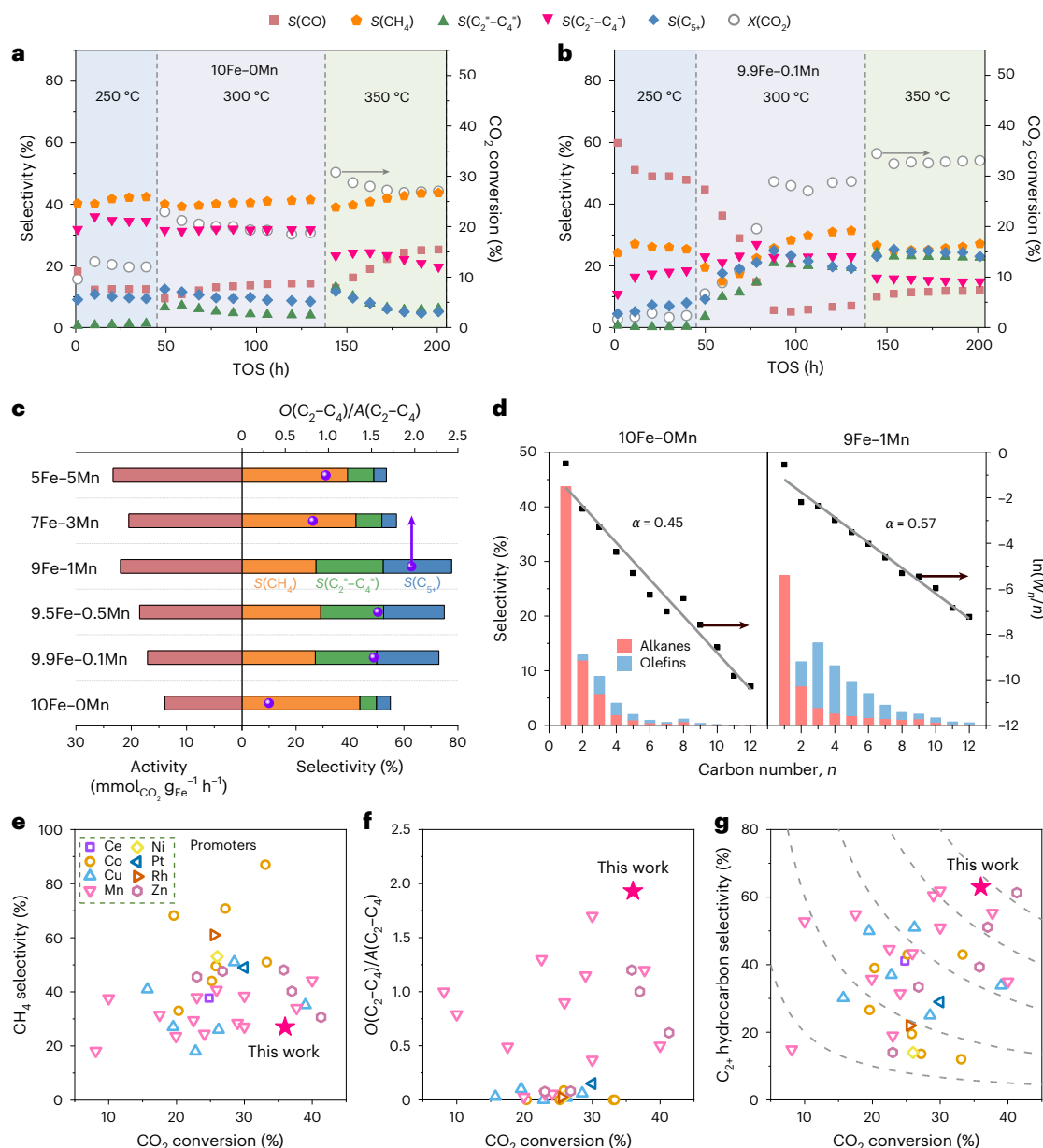


**Fig. 1 | Comparative performance of Fe-based catalysts in CO<sub>2</sub> hydrogenation.** **a,b**, The evolution of CO<sub>2</sub> conversion (right axis) and product selectivity (left axis) over 10Fe-0Mn (**a**) and 9.9Fe-0.1Mn (**b**) at different reaction temperatures (*T*) as a function of the time on stream (TOS). The catalysts were tested for CO<sub>2</sub> hydrogenation at a pressure (*P*) of 15 bar and *T* = 250, 300 and 350 °C for about 200 h on stream in total. **c**, The Fe-related integral rate of CO<sub>2</sub> consumption (bottom left axis), selectivity data (bottom right axis) for methane (*S*(CH<sub>4</sub>), orange), light olefins (*S*(C<sub>2</sub><sup>+</sup>-C<sub>4</sub><sup>+</sup>), green) and C<sub>5</sub><sup>+</sup> hydrocarbons (*S*(C<sub>5</sub><sup>+</sup>), blue) and the ratio of light olefins to light alkanes (top right axis; *O*(C<sub>2</sub>-C<sub>4</sub>)/*A*(C<sub>2</sub>-C<sub>4</sub>), purple points) obtained at 350 °C over *x*Fe-*y*Mn catalysts. **d**, Selectivity for individual hydrocarbons (left axis; coloured bars) and Anderson-Schulz-Flory plot (right axis; black points) for 10Fe-0Mn (left) and 9Fe-1Mn (right) catalysts,

with their associated  $\alpha$ -values. For **a-d**, the reaction conditions are:  $m_{\text{cat}} = 0.1$  g,  $T = 200-350$  °C (**a,b**) or  $T = 350$  °C (**c,d**),  $P = 15$  bar, gas hourly space velocity = 3,600 ml g<sub>cat</sub><sup>-1</sup> h<sup>-1</sup> and CO<sub>2</sub>:H<sub>2</sub>:N<sub>2</sub> = 1:3:0.3. The catalysts were initially reduced in the 50 vol% H<sub>2</sub>/N<sub>2</sub> at the same pressure and 400 °C for 2 h. **e-g**, Comparison of the 9Fe-1Mn catalyst with previously reported Fe-based catalysts promoted with a transition metal (Ce, Co, Cu, Mn, Ni, Pt, Rh, Zn) in terms of *S*(CH<sub>4</sub>) (**e**), *O*(C<sub>2</sub>-C<sub>4</sub>)/*A*(C<sub>2</sub>-C<sub>4</sub>) (**f**) and *S*(C<sub>2</sub><sup>+</sup>) (**g**) as a function of CO<sub>2</sub> conversion. The dashed grey lines in **g** stand for the yield of C<sub>2</sub><sup>+</sup> hydrocarbons of 2, 6, 12, 18 and 24% (from bottom left to top right). The key to the symbols in **e** also applies to **f** and **g**. Details of the catalyst formulations and reaction conditions are provided in Supplementary Table 2.

time- and temperature-resolved characterization studies, mechanistic and kinetic analyses of product formation and density functional theory (DFT) calculations.

### Spatially resolved steady-state kinetic analysis

The effect of Mn content on the progress of CO<sub>2</sub>-FTS, that is, product formation along the catalyst bed (Fig. 2a), was explained by analysing the segmental rates of overall CO<sub>2</sub> consumption ( $r_s(\text{CO}_2)$ ), CH<sub>4</sub> formation

( $r_s(\text{CH}_4)$ ) and C<sub>2</sub><sup>+</sup> hydrocarbon formation ( $r_s(\text{C}_{2+})$ ) (Supplementary Note 3). Despite the lower  $r_1(\text{CO}_2)$  determined in the first 5% upstream layer (the first segment), Mn-containing catalysts possess higher activity in the remaining 80% downstream layers (Fig. 2b). Importantly,  $r_1(\text{CH}_4)$  was strongly suppressed by Mn (Fig. 2c). In contrast to 10Fe-0Mn, catalysts 9.9Fe-0.1Mn, 9.5Fe-0.5Mn and 9Fe-1Mn showed substantial activity to produce C<sub>2</sub><sup>+</sup> hydrocarbons over the whole bed (Fig. 2d and Supplementary Fig. 8). According to our previous results<sup>43,44</sup>, the strong decrease in

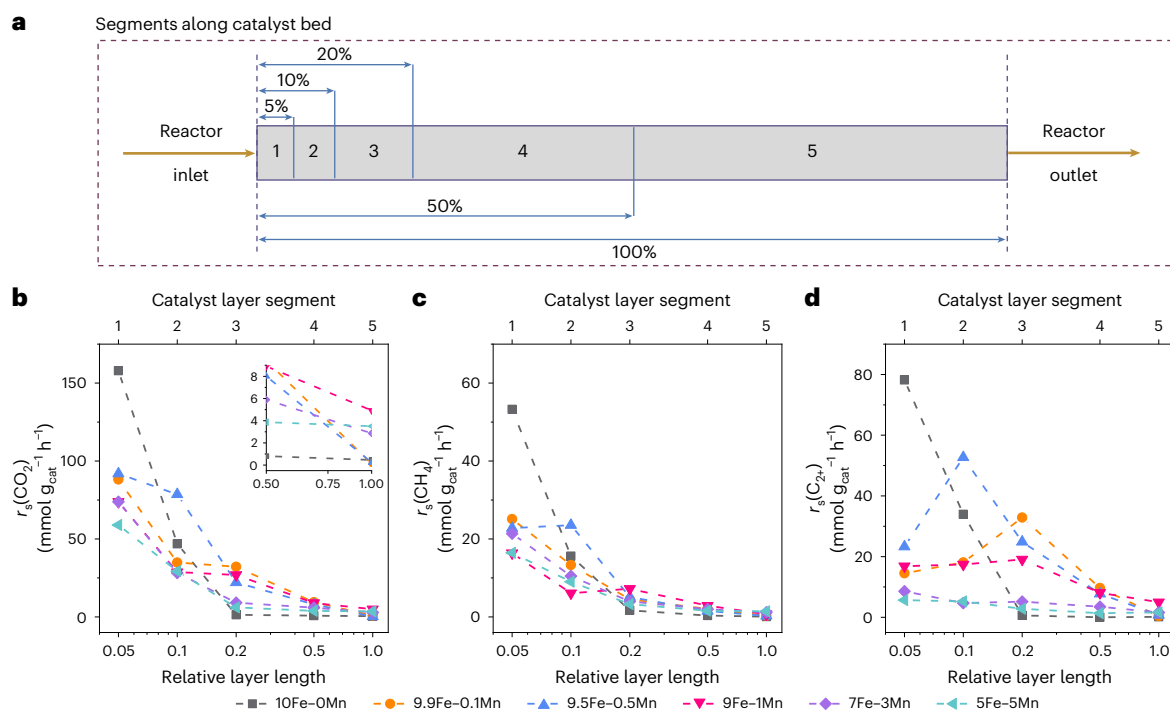


**Fig. 2 | Spatially resolved kinetic analysis of CO<sub>2</sub> conversion and product formation.** **a**, Schematic representation of the segments along the catalyst bed. The longest bed contains 100 mg catalyst. **b–d**, Segmental rates of overall CO<sub>2</sub> consumption ( $r_s(\text{CO}_2)$ ) (**b**), CH<sub>4</sub> formation ( $r_s(\text{CH}_4)$ ) (**c**) and C<sub>2+</sub> hydrocarbon formation ( $r_s(\text{C}_{2+})$ ) (**d**) over the different xFe–yMn catalysts. The insert in **b**

shows the rate of CO<sub>2</sub> consumption in the 5th segment, that is, between 0.5 and 1.0 relative layer length. The methodology of calculating the segmental rates is described in Supplementary Note 3. Reaction conditions:  $T = 350^\circ\text{C}$ ,  $P = 15$  bar and  $\text{CO}_2:\text{H}_2:\text{N}_2 = 1:3:0.3$ .

$r_s(\text{C}_{2+})$  over 10Fe–0Mn from segment to segment can be explained by the absence of iron carbide  $\text{Fe}_5\text{C}_2$  in the downstream layers. In this view,  $\text{Fe}_5\text{C}_2$  in the Mn-containing catalysts with an Mn/Fe atomic ratio of 0.01–0.11 should be present practically along the whole bed due to the positive effect of Mn on the stability of  $\text{Fe}_5\text{C}_2$  against oxidation by  $\text{CO}_2/\text{H}_2\text{O}$ .

On the basis of the selectivity–conversion relationships obtained for CO, CH<sub>4</sub> and C<sub>2+</sub> hydrocarbons over each of the catalysts under isothermal conditions (Supplementary Fig. 9), CO and CH<sub>4</sub> were identified as the primary products (Supplementary Fig. 10 and Supplementary Note 4). The lowest contribution of CO<sub>2</sub> methanation to the overall CO<sub>2</sub> conversion was determined over 9Fe–1Mn. In addition, the presence of Mn inhibited the hydrogenation of lower olefins, as demonstrated by the dependence of the selectivity for these products on CO<sub>2</sub> conversion (Supplementary Fig. 11 and Supplementary Note 4).

Throughout the discussion above, the presence of Mn is critical in inhibiting direct CO<sub>2</sub> methanation and olefin hydrogenation reactions in CO<sub>2</sub>-FTS. Furthermore, this promoter helps to achieve a more homogeneous distribution of catalytically active iron carbides along the catalyst bed.

### Mn-modulated catalyst restructuring

To derive mechanistic and kinetic insights into the effects of Mn and its content on catalyst reducibility, in situ XAS experiments were performed in a temperature-programmed manner (Supplementary Fig. 12). The phase composition was determined via linear combination analysis (LCA) of X-ray absorption near-edge structure (XANES) spectra at the Fe K edge (Fig. 3).  $\alpha\text{-Fe}_2\text{O}_3$  in the 10Fe–0Mn catalyst was stable up to  $\sim 360^\circ\text{C}$  and was reduced to  $\text{Fe}_3\text{O}_4$  at higher temperatures (Fig. 3a,b and Supplementary Fig. 13). The reduction of the latter phase to metallic Fe occurred at  $385^\circ\text{C}$ . To mimic the reduction procedure used before CO<sub>2</sub>-FTS tests, the reduction process at  $400^\circ\text{C}$  lasted for two hours. After this, the reduced 10Fe–0Mn catalyst contained only metallic Fe (Supplementary Fig. 14).

In comparison with 10Fe–0Mn, the onset of reduction of 9Fe–1Mn and 7Fe–3Mn shifted to a lower temperature, that is, around  $280^\circ\text{C}$  and  $205^\circ\text{C}$ , respectively (Fig. 3c–f). Moreover, both  $\text{Fe}_3\text{O}_4$  and FeO co-existed during the reduction process (Fig. 3d,f). Although it has been reported that the FeO phase is unstable below  $590^\circ\text{C}$  (refs. 26,45), the presence of FeO in our experiments can be explained by the incorporation of  $\text{Mn}^{2+}$  into the FeO lattice, resulting in the formation of  $\text{Mn}_{1-x}\text{Fe}_x\text{O}$  solid solution<sup>26,27</sup>. This intermediate is stable against reduction up to  $400^\circ\text{C}$ , at which temperature metallic Fe was formed gradually with increasing time on the  $\text{H}_2$  stream (Supplementary Figs. 15–18). After two hours at  $400^\circ\text{C}$ , 9Fe–1Mn contained metallic Fe (76%) and  $\text{Mn}_{1-x}\text{Fe}_x\text{O}$  (24%). The reduced 7Fe–3Mn had a similar composition. The oxidation state of Mn in the reduced 9Fe–1Mn and 7Fe–3Mn is  $2+$ , as concluded from in situ XANES and EXAFS spectra at the Mn K edge (Supplementary Fig. 19) and XPS spectra (Supplementary Fig. 20). These results, complemented by X-ray diffraction (XRD) analysis (Supplementary Fig. 21), confirmed the inhibiting effect of Mn on the reduction of  $\text{Fe}_3\text{O}_4/\text{FeO}$  due to the formation of stable  $\text{Mn}_{1-x}\text{Fe}_x\text{O}$ .

In situ XAS tests were further performed to scrutinize catalyst restructuring under CO<sub>2</sub>-FTS conditions (Supplementary Fig. 12). The fraction of metallic Fe in 10Fe–0Mn decreased with increasing reaction temperature starting from  $120^\circ\text{C}$ , whereas the fraction of  $\text{Fe}_5\text{C}_2$  increased and reached around 50% at  $300^\circ\text{C}$  (Fig. 4a,b and Supplementary Figs. 22 and 23). A further increase to 80% was achieved after two hours on the CO<sub>2</sub>-FTS stream (Fig. 4b). The predominantly carbidic nature of Fe in the 10Fe–0Mn catalyst is further supported by the in situ EXAFS spectroscopy results (Fig. 4c).

When the reduced 9Fe–1Mn catalyst was exposed to the CO<sub>2</sub>-FTS feed,  $\text{Fe}_5\text{C}_2$  was detected already at  $60^\circ\text{C}$ , whereas metallic Fe had disappeared (Fig. 4d,e and Supplementary Figs. 24 and 25). The fraction of  $\text{Mn}_{1-x}\text{Fe}_x\text{O}$  decreased with increasing temperature and approached zero at  $235^\circ\text{C}$ . However,  $\text{Fe}_5\text{C}_2$  was not stable above  $150^\circ\text{C}$ , where this compound and  $\text{Mn}_{1-x}\text{Fe}_x\text{O}$  were probably oxidized to  $\text{Fe}_3\text{O}_4$ . A new



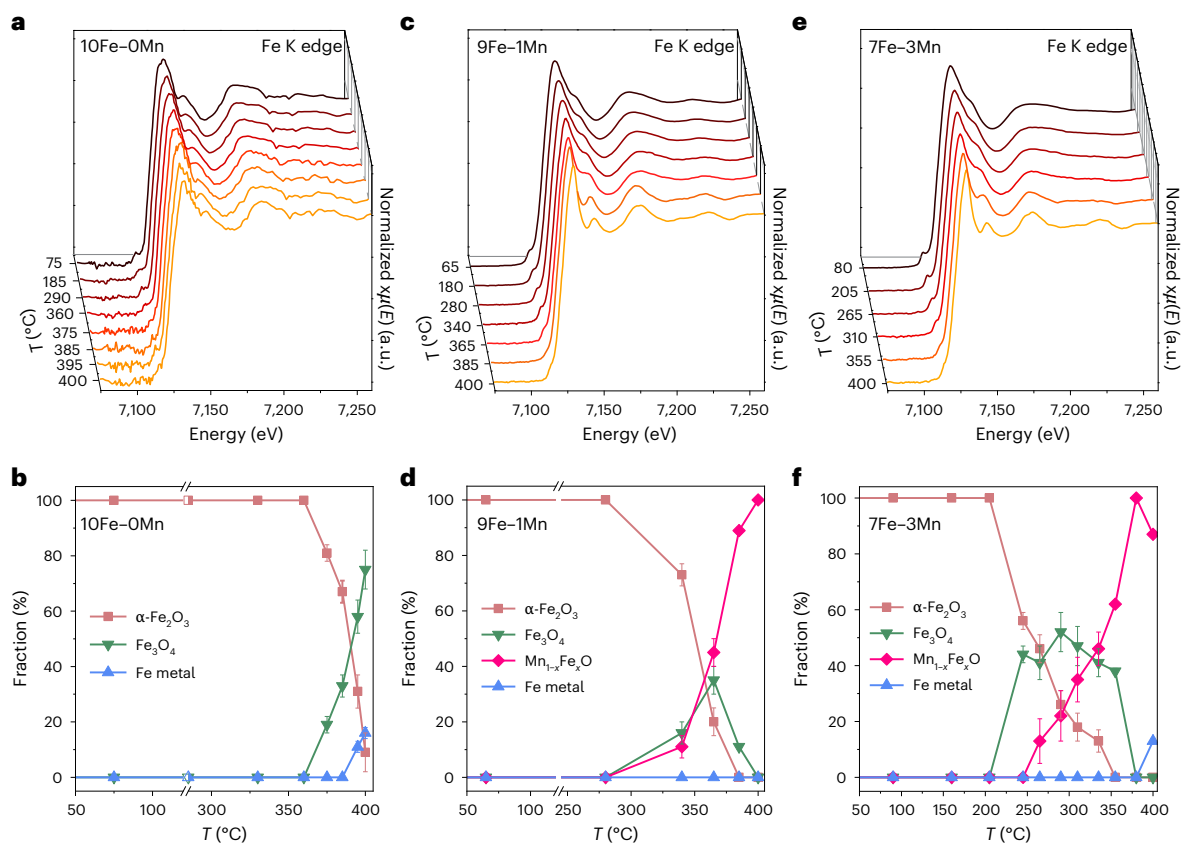


**Fig. 3 | Reduction behaviour of catalysts studied using in situ XAS. a–f**, In situ XANES spectra at the Fe K edge measured during temperature-programmed reduction of  $x\text{Fe}-y\text{Mn}$  catalysts at 15 bar in a 50 vol%  $\text{H}_2/\text{N}_2$  flow (Supplementary Fig. 12) (a, c and e) and evolution of the fraction of Fe species determined via

LCA analysis of the corresponding XANES spectra (b, d and f) for 10Fe-0Mn (a,b), 9Fe-1Mn (c,d) and 7Fe-3Mn (e,f). The error bars in b, d and f represent the standard error of the weight coefficients obtained from LCA using 64 data points.

phase, manganese ferrite ( $\text{Mn}_x\text{Fe}_{3-x}\text{O}_4$ ), appeared at 300 °C, as also shown by the in situ XANES spectra at the Mn K edge (Supplementary Figs. 26a and 27a and Supplementary Note 5). Mn in this phase has an average oxidation state higher than 2+. No substantial changes in the composition of the catalyst were observed during cooling from 300 to 25 °C (Fig. 4f and Supplementary Fig. 28).

Bearing in mind the dynamic performance of the 9Fe-1Mn catalyst in  $\text{CO}_2$ -FTS at 300 °C but a stable operation at 350 °C (Supplementary Fig. 2b), additional in situ XANES tests were carried out as follows. After cooling from 300 °C to room temperature, the catalyst was heated to 350 °C and operated for two hours. At temperatures above 300 °C,  $\text{Mn}_x\text{Fe}_{3-x}\text{O}_4$  began to transform into  $\text{Fe}_3\text{O}_4$  and  $\text{Mn}_{1-x}\text{Fe}_x\text{O}$  (Fig. 4g,h and Supplementary Figs. 29 and 30). Correspondingly, the oxidation state of Mn was reduced to 2+, as indicated by the in situ XANES spectrum at the Mn K edge after 2 h on  $\text{CO}_2$ -FTS stream at 350 °C (Supplementary Figs. 26b and 27b and Supplementary Note 5). The formation of  $\text{Fe}_3\text{C}_2$  occurred at 350 °C and its fraction increased with increasing time on stream. As the fraction of  $\text{Fe}_3\text{O}_4$  decreased accordingly, while metallic Fe was not observed, we put forward that this iron oxide was directly converted into  $\text{Fe}_3\text{C}_2$ . Decreasing the temperature from 350 to 25 °C led to a slight re-oxidation of  $\text{Fe}_3\text{C}_2$  (Supplementary Fig. 31). The final in situ EXAFS spectrum also indicates that iron oxides are dominant in the catalyst (Fig. 4i).

Summarising, the formation of catalytically active  $\text{Fe}_3\text{C}_2$  in Mn-containing catalysts is not favourable below 300 °C due to their low reducibility. Consequently, they require longer induction periods and higher reaction temperatures to achieve a steady-state performance in comparison to 10Fe-0Mn. Further insights into reaction-induced catalyst restructuring are given below.

### Structural characterization of spent catalysts

On the basis of the XPS spectra of Mn 2p (Fig. 5a) and Mn 3s (Supplementary Fig. 32), the oxidation state of Mn in all Mn-containing spent catalysts after 200 h on reaction stream is 2+. The binding energy of Fe, however, shifts from 710.8 to 710.3 eV with an increase in Mn content (Supplementary Fig. 33), probably due to the electron donation from MnO to Fe component(s). The steady-state composition (Fig. 5b and Supplementary Table 3) of the spent catalysts depends on the Mn loading, as determined by analysing XRD patterns (Supplementary Figs. 34 and 35). The highest fraction of  $\text{Fe}_3\text{C}_2$  was identified in the spent 9Fe-1Mn catalyst, although its fresh counterpart forms  $\text{Fe}_3\text{C}_2$  more slowly in comparison with 10Fe-0Mn (Fig. 4). This result was further supported by the analysis of ex situ XANES and EXAFS spectra of the spent catalysts (Supplementary Figs. 36 and 37).

The spent 9Fe-1Mn catalyst after 200 h on the reaction stream was further characterized using annular dark-field scanning transmission electron microscopy (ADF-STEM) and EELS. The ADF-STEM image revealed a core-shell structure with a shell thickness of less than 10 nm (Fig. 5c). The local elemental composition was investigated via EELS spectrum imaging. The carbon K-edge EELS spectrum in region 2 (core part) displayed distinctive fine structure (Fig. 5d), showing an intense pre-peak (~286 eV)<sup>46</sup>. In other regions, however, features similar to amorphous carbon species (~297 eV) were observed. Therefore, the core part was composed mainly of iron carbide phase, supported by the absence of Mn and low O signals in the EELS spectrum of region 2 (Fig. 5d) and visualized by the EELS maps (Fe-L C, C-K C; Fig. 5e,f). In the shell part (region 1), both Fe L-edge and Mn L-edge features were observed with the presence of an O signal, suggesting the existence of mixed Fe-Mn oxide.  $\text{MnO}_x$  species with different Fe contents were also found in some

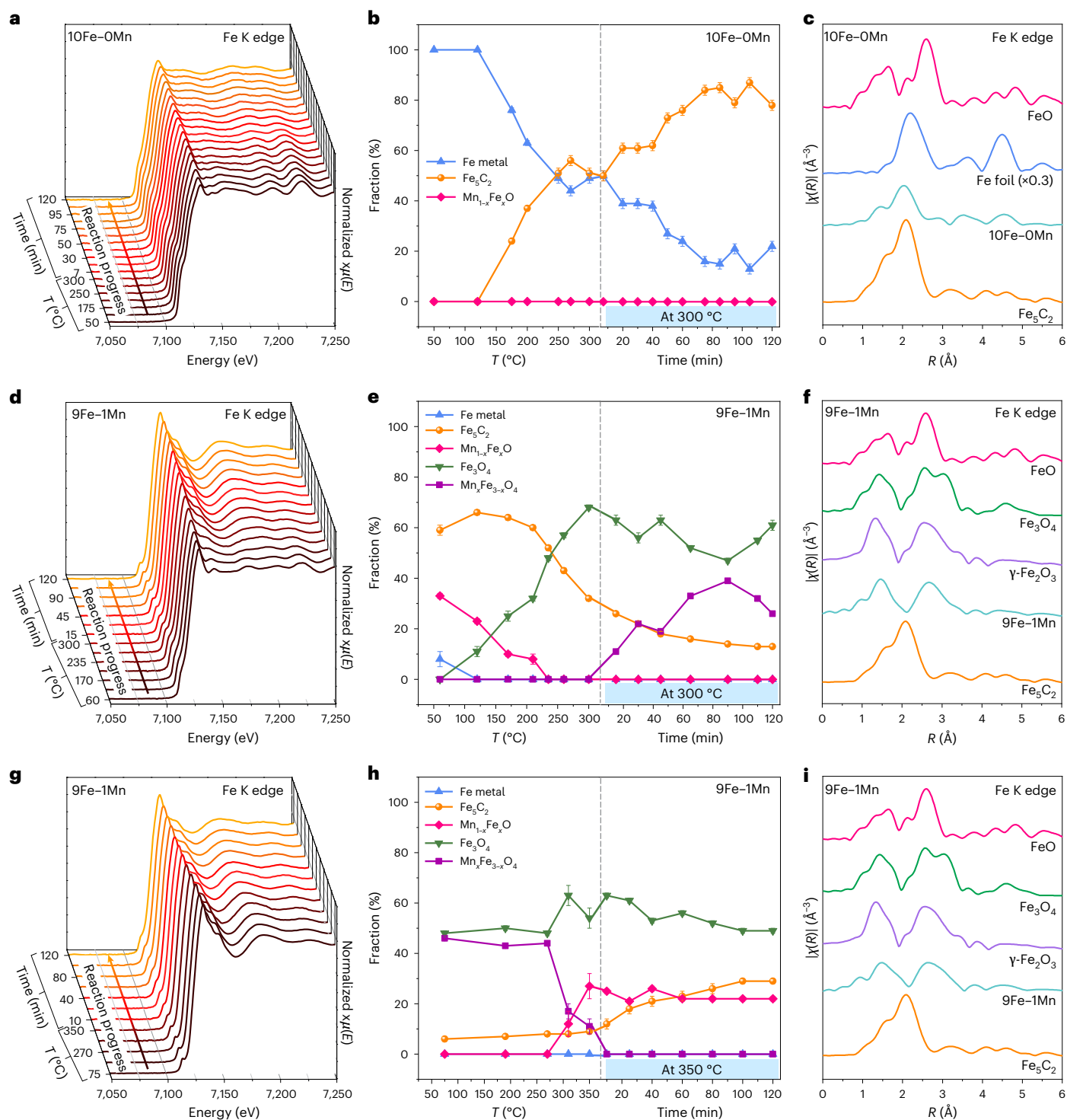


**Fig. 4 | Iron speciation under the reaction conditions. a–i,** Time-resolved in situ XANES spectra of  $x\text{Fe}–y\text{Mn}$  catalysts at the Fe K edge (**a,d,g**) collected at different temperatures and 15 bar in a CO<sub>2</sub>:H<sub>2</sub>:N<sub>2</sub> = 1:3:6 feed (Supplementary Fig. 12), evolution of the Fe species determined via LCA analysis of the corresponding

XANES spectra (**b,e,h**) and in situ  $k^2$ -weighted Fourier-transformed EXAFS spectra (collected after the reaction) in Rspace (**c,f,i**) for 10Fe-0Mn (**a,b**) and 9Fe-1Mn (**d,e,g,h**). The bars in **b,e** and **h** represent the standard error of the weight coefficients obtained from LCA using 64 data points.

regions in the vicinity of iron carbides (regions 3 and 4 in Fig. 5c,d). The detailed location of each component can be seen in the EELS maps with their chemical information (Fig. 5e,f). Here, the presence of a carbon interfacial layer between iron carbides and iron oxides may be of note.

Combining the results of the catalytic tests and characterization of the catalysts at different life stages, we put forward that the MnO-containing overlay surrounding the Fe<sub>5</sub>C<sub>2</sub> surface plays a crucial

role in optimizing the product selectivity and stabilizing Fe<sub>5</sub>C<sub>2</sub>. Having identified the effects of Mn on the reaction-induced restructuring and CO<sub>2</sub>-FTS performance, we now focus on the fundamentals behind them.

**Mechanistic and kinetic insights into the role of Mn in CO<sub>2</sub>-FTS**  
The interactions of CO<sub>2</sub>, H<sub>2</sub> and C<sub>2</sub>H<sub>4</sub> with the spent catalysts were investigated at 350 °C using a temporal analysis of products (TAP-2)

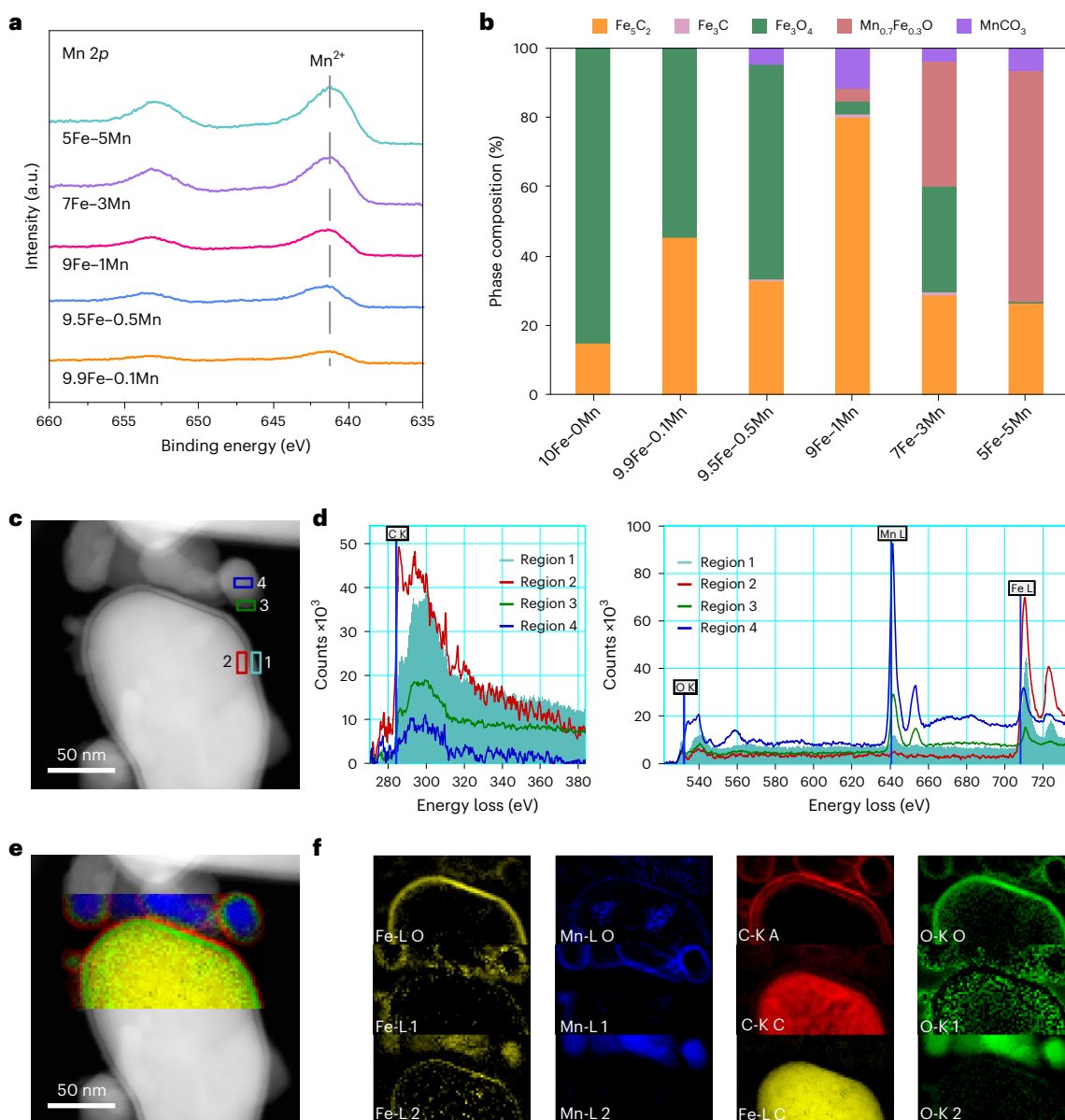


**Fig. 5 | Structural characterization and visualization of the spent catalysts.**

**a**, Mn 2p XPS spectra of the spent catalysts collected after 200 h on stream. **b**, Phase composition of the spent catalysts based on the Rietveld quantitative phase analysis of their XRD patterns (Supplementary Figs. 34 and 35). **c,d**, Representative ADF-STEM image of spent 9Fe-1Mn (**c**) and the STEM-EELS spectra (**d**) extracted from the spectrum imaging dataset for regions 1–4 indicated in **c**. **e,f**, ADF-STEM image with an overlaid EELS map (iron carbide, yellow; manganese, blue; oxygen from iron oxide, green; carbon, red) (**e**) and

EELS elemental maps (**f**). In **f**, A denotes amorphous carbon, C represents carbide carbon and iron, O indicates the iron oxide layer (region 1) with manganese as a minority phase, 1 denotes manganese oxide type 1 (region 3) with iron as a minority element, and 2 indicates manganese oxide type 2 (region 4) also with iron as a minority element. Note that in using the near-edge fine structures of the different elements from separate locations as a model for a fitting algorithm, maps of the electronic states of the different elements have been calculated.

reactor. For all of the catalysts tested, the dimensionless CO<sub>2</sub> response crosses that of argon (Ar) (Supplementary Fig. 38), which is a fingerprint of reversible CO<sub>2</sub> adsorption. Thus, various microkinetic models of CO<sub>2</sub> activation that considers reversible adsorption were developed (Supplementary Table 4) and used to describe the experimental (non-dimensionless) CO<sub>2</sub> responses (see Supplementary Methods). The model assuming a reversible and dissociative CO<sub>2</sub> adsorption provided the best fit (Supplementary Fig. 39 and Supplementary Table 5). The sensitivity and correlation analyses of the obtained kinetic parameters justify their reliability (Supplementary Tables 6 and 7).

An effective rate constant of CO<sub>2</sub> adsorption ( $k_{\text{ads}}^{\text{eff}}(\text{CO}_2)$ ) seems to pass through a maximum with increasing Mn content (Fig. 6a and Supplementary Table 6), whereas the rate constant for desorption of

adsorbed CO<sub>2</sub> ( $k_{\text{des}}(\text{CO}_2)$ ) decreases (Supplementary Fig. 40a). Consequently, the equilibrium constant of CO<sub>2</sub> adsorption, which is expressed as  $k_{\text{ads}}^{\text{eff}}(\text{CO}_2)/k_{\text{des}}(\text{CO}_2)$  increases (Fig. 6b), indicating that Mn enhances the strength of CO<sub>2</sub> adsorption. The highest rate constant of dissociation of adsorbed CO<sub>2</sub> ( $k_{\text{diss}}^{\text{eff}}(\text{CO}_2)$ ) was determined for 9Fe-1Mn (Supplementary Fig. 40b). The intrinsic rates of CO<sub>2</sub> consumption and CH<sub>4</sub> formation in CO<sub>2</sub>-FTS appear to decrease with increasing  $k_{\text{ads}}^{\text{eff}}(\text{CO}_2)/k_{\text{des}}(\text{CO}_2)$  (Fig. 6c and Supplementary Fig. 41). This tendency for  $r_1(\text{CO}_2)$  suggests that strongly adsorbed CO<sub>2</sub>-related species are difficult to be converted into CO and CH<sub>4</sub>.

The ability of the catalyst to activate H<sub>2</sub>, as determined from hydrogen–deuterium (H/D) exchange experiments, decreases with the content of Mn (Fig. 6d and Supplementary Fig. 42). Therefore, we put

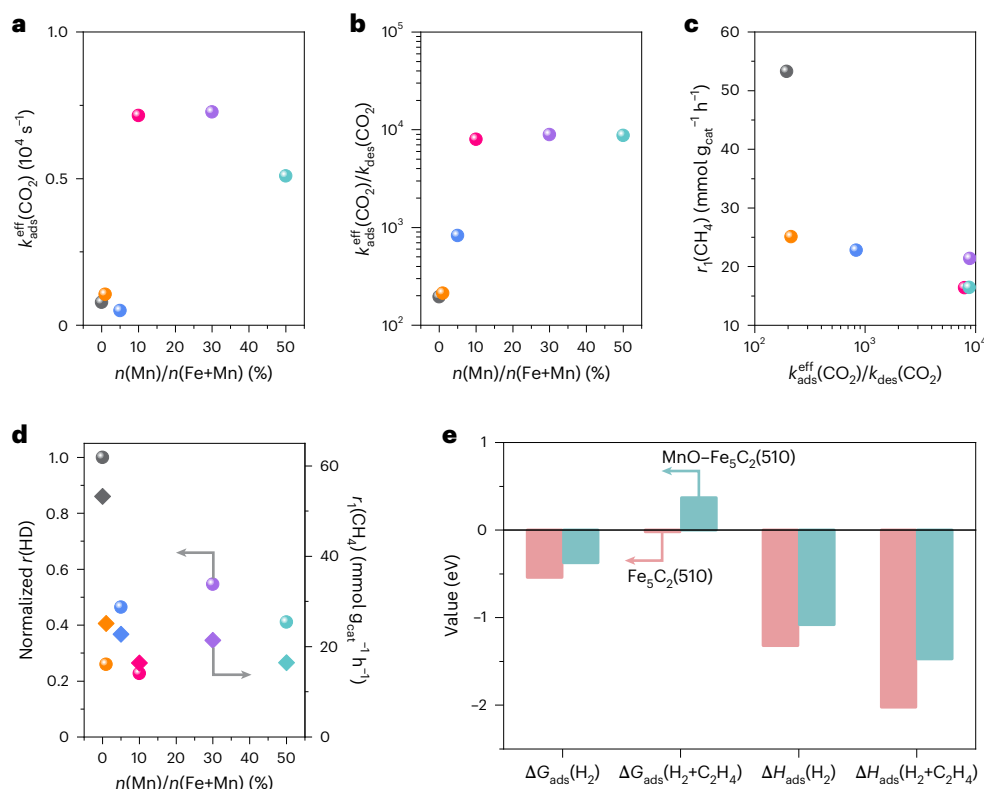


**Fig. 6 | Kinetic analysis and performance descriptor of  $x\text{Fe}-y\text{Mn}$  catalysts in  $\text{CO}_2$ -FTS.** **a,b**, The rate constant of  $\text{CO}_2$  adsorption ( $k_{\text{ads}}^{\text{eff}}(\text{CO}_2)$ ) (**a**) and the equilibrium constant of  $\text{CO}_2$  adsorption ( $k_{\text{ads}}^{\text{eff}}(\text{CO}_2)/k_{\text{des}}(\text{CO}_2)$ ) (**b**) determined by fitting  $\text{CO}_2$  responses to a reversible and dissociative  $\text{CO}_2$  adsorption model (model 4 in Supplementary Table 4) as a function of Mn content in the catalysts. **c**, The rate of  $\text{CH}_4$  formation determined in the first segment ( $r_1(\text{CH}_4)$ ) shown in

Fig. 2) as a function of  $k_{\text{ads}}^{\text{eff}}(\text{CO}_2)/k_{\text{des}}(\text{CO}_2)$ . **d**, The normalized HD formation rate determined by H/D exchange experiments and  $r_1(\text{CH}_4)$  as a function of Mn content in the catalysts. **e**, Relative Gibbs free energy of adsorption ( $\Delta G_{\text{ads}}$ ) and enthalpy of adsorption ( $\Delta H_{\text{ads}}$ ) of  $\text{H}_2$  and  $\text{C}_2\text{H}_4$  on  $\text{Fe}_3\text{C}_2(510)$  and  $\text{MnO-Fe}_3\text{C}_2(510)$  surfaces under the reaction conditions ( $T = 350^\circ\text{C}$ ,  $P = 15$  bar and  $\text{CO}_2:\text{H}_2:\text{N}_2 = 1:3:0.3$ ).

forward that the surface ratio of C/H should increase with increasing Mn content. This conclusion is substantiated by the same tendency of  $r_1(\text{CH}_4)$  and the HD (hydrogen deuteride) formation rate as a function of Mn content (Fig. 6d) and highlights that an optimal surface C/H ratio is required for achieving the selective production of olefins and lowering the selectivity for  $\text{CH}_4$ . Furthermore, pulse experiments with  $\text{C}_2\text{H}_4:\text{Ar} = 1:1$  (Supplementary Fig. 43) suggest that catalyst promotion with Mn diminishes the adsorption of this olefin, especially on 9Fe-1Mn. This should be the reason for the highest  $O(\text{C}_2-\text{C}_4)/A(\text{C}_2-\text{C}_4)$  ratio achieved over this catalyst in  $\text{CO}_2$ -FTS (Fig. 1c).

In summary, the promoter Mn seems to affect the adsorption/activation of  $\text{CO}_2$ ,  $\text{H}_2$  and  $\text{C}_2\text{H}_4$ , which are relevant to the catalyst performance. The DFT calculations described below rationalize these effects.

### Experimentally guided computational study

We also performed DFT calculations for  $\text{CO}_2/\text{H}_2$  activation and  $\text{C}_2\text{H}_4$  hydrogenation as a model reaction for the hydrogenation of olefins using the  $\text{Fe}_3\text{C}_2(510)$  and  $\text{MnO-Fe}_3\text{C}_2(510)$  surface models (Supplementary Fig. 44), which represent the unpromoted and Mn-promoted catalysts, respectively. These models were constructed on the basis of the experimental results and surface atomic ratio of Mn/Fe for the best-performing 9Fe-1Mn catalyst (Fig. 5 and Supplementary Table 1; see Methods for details). In agreement with the experimental results of  $\text{CO}_2$  activation in Fig. 6a,b, the calculations predict an increase in the strength of  $\text{CO}_2$  adsorption in the presence MnO (Supplementary Fig. 45 and Supplementary Table 8). This was rationalized by the involvement of the interfacial sites between MnO and  $\text{Fe}_3\text{C}_2$  during the adsorption process.

$\text{H}_2$  activation on the  $\text{Fe}_3\text{C}_2(510)$  surface occurs on the Fe sites; it is exergonic by 0.54 eV and does not have any activation barrier (Supplementary Fig. 46), indicating a spontaneous dissociation. Both the Fe sites and the periphery of the Mn-O interfacial sites on the  $\text{MnO-Fe}_3\text{C}_2(510)$  surface can be involved in the formation of surface species from  $\text{H}_2$  with the Gibbs free energy barrier values of 0.30 and 0.31 eV, respectively. This should be the reason for the negative effect of Mn on  $\text{H}_2$  activation as shown by the H/D exchange experiments (Fig. 6d).

The presence of Mn was not found to be essential for the Gibbs free energy, enthalpy and energy profiles and the apparent Gibbs free energy barrier in  $\text{C}_2\text{H}_4$  hydrogenation (Supplementary Figs. 47–49 and Supplementary Table 9). However, on the basis of the adsorption Gibbs free energy ( $\Delta G_{\text{ads}}$ ) and adsorption enthalpy ( $\Delta H_{\text{ads}}$ ) under the reaction conditions, the  $\text{MnO-Fe}_3\text{C}_2(510)$  surface has a lower affinity for binding  $\text{H}_2$  and  $\text{C}_2\text{H}_4$  in comparison with the  $\text{Fe}_3\text{C}_2(510)$  surface (Fig. 6e and Supplementary Table 10), as also concluded via TAP analysis of the  $\text{C}_2\text{H}_4$  interaction with unpromoted and Mn-promoted catalysts (Supplementary Fig. 43). The weakened activity of the  $\text{MnO-Fe}_3\text{C}_2(510)$  surface, compared with the  $\text{Fe}_3\text{C}_2(510)$  surface, towards adsorption/activation of  $\text{H}_2$  and  $\text{C}_2\text{H}_4$  was further supported by the projected density of states and Bader charge analyses with an adsorbed H atom and  $\text{C}_2\text{H}_4$  on both surfaces (Supplementary Figs. 50 and 51 and Supplementary Note 6).

### Conclusions

Rather than simply focusing on the identification of the steady-state catalyst composition, this work was aimed primarily at elucidating the role of the Mn promoter in the surface and bulk dynamics of  $\text{Fe}_2\text{O}_3$ -based



catalysts during their preconditioning and operation in CO<sub>2</sub>-FTS. The presence of Mn lowers the rates of reduction and carburization processes, especially at low temperatures (<300 °C). These effects result in an apparent reaction-induced and Mn concentration-modulated evolution of catalytically active phases and accordingly the CO<sub>2</sub>-FTS performance. An optimal Mn loading is required to form in situ Fe<sub>3</sub>C<sub>2</sub> active assemblies with a MnO-containing surface layer, selectively producing light olefins and C<sub>5+</sub> hydrocarbons. This is due to hindering CH<sub>4</sub> formation through CO<sub>2</sub> methanation, as revealed by spatially resolved kinetic analysis of the product formation in CO<sub>2</sub>-FTS. Based on the microkinetic analysis and DFT calculations for CO<sub>2</sub>, H<sub>2</sub> and C<sub>2</sub>H<sub>4</sub> activation, the promotional effect of Mn can be rationalized by an interplay of the kinetics of the generation of surface species from CO<sub>2</sub>, H<sub>2</sub> and C<sub>2</sub>H<sub>4</sub>. The knowledge gained and the methodology introduced can be valuable in establishing property–performance relationships and enabling the targeted design of catalysts for use beyond CO<sub>2</sub> hydrogenation.

## Methods

### Catalyst preparation

A series of  $x\text{Fe}-y\text{Mn}$  catalysts, with different Fe/Mn molar ratios, was prepared via the co-precipitation method using iron(III) nitrate nonahydrate (Fe(NO<sub>3</sub>)<sub>3</sub>·9H<sub>2</sub>O) and manganese(II) nitrate tetrahydrate (Mn(NO<sub>3</sub>)<sub>2</sub>·4H<sub>2</sub>O) as the metal precursors. Typically, appropriate amounts of Fe(NO<sub>3</sub>)<sub>3</sub>·9H<sub>2</sub>O and Mn(NO<sub>3</sub>)<sub>2</sub>·4H<sub>2</sub>O were dissolved in deionized water (180 ml) for a total molar concentration of Fe<sup>3+</sup> and Mn<sup>2+</sup> of 0.56 mol l<sup>-1</sup>. Each mass of Fe(NO<sub>3</sub>)<sub>3</sub>·9H<sub>2</sub>O and Mn(NO<sub>3</sub>)<sub>2</sub>·4H<sub>2</sub>O was determined by the molar ratio of Fe to Mn (9.9:0.1, 9.5:0.5, 9:1, 7:3 and 5:5). The mixture was stirred at room temperature for 1 h. Then, ammonia solution (NH<sub>4</sub>OH; Roth, 25% NH<sub>3</sub> in H<sub>2</sub>O) was added dropwise into the above solution under stirring until the pH value reached 9.5. The suspension was aged for 3 h, filtered and washed until a neutral pH value was achieved. The obtained samples were dried at 100 °C overnight and calcined at 400 °C with a heating rate of 3 °C min<sup>-1</sup> for 6 h. They were named  $x\text{Fe}-y\text{Mn}$ , where  $x:y$  stands for the molar ratio of Fe to Mn. The catalyst without Mn was also prepared using only Fe(NO<sub>3</sub>)<sub>3</sub>·9H<sub>2</sub>O while other preparation conditions were kept the same.

### Catalyst characterization

XRD powder patterns were recorded using a Stoe Stadi P transmission diffractometer equipped with a DECTRIS Mythen2 IK detector applying Ge(111) monochromatized Mo K $\alpha$ 1 radiation (50 kV, 40 mA and 0.70930 Å). The sample was ground to a fine powder and placed between two acetate foils before the XRD measurements were carried out. Data acquisition parameters were adapted to the sample scattering properties. Peak positions and profiles were fitted with the pseudo-Voigt function using the HighScore Plus software package (Panalytical). Phase identification was carried out using the PDF-2 database of the International Centre of Diffraction Data 2016. The size of the Fe<sub>2</sub>O<sub>3</sub> crystallites was determined according to the Scherrer equation using (012), (104), (110), (113), (024) and (116) reflexes, and an average value was reported. Quantitative phase analysis was performed using the Rietveld method in HighScore plus, with details provided in Supplementary Note 7.

Inductively coupled plasma optical emission spectroscopy (ICP-OES) was conducted using a Varian 715-ES ICP optical emission spectrometer. Each sample (~0.01 g) was mixed with aqua regia (8 ml). The sample preparation system (Multiwave PRO, Anton Paar) was operated at 220 °C and 50 bar for the sample digestion with a microwave-assisted method. The digested solution was diluted to 100 ml and measured using ICP-OES. The data analysis was carried out using the ICP Expert 715-ES software.

Nitrogen sorption was measured at 77 K using a Micromeritics ASAP 2020 instrument. The specific surface area was evaluated according to the Brunauer–Emmett–Teller method. Before the measurements,

the samples (250–450 µm, 0.1 g) were degassed at 250 °C under vacuum for 2 h.

Raman microspectroscopic investigations were performed using a Renishaw inVia Raman microscope. A spatula tip of the sample was placed on a microscope slide and a 633 nm laser light was used with a laser power of 0.17–1.7 mW.

XPS measurements were carried out using ESCALAB 220iXL apparatus equipped with monochromated Al K $\alpha$  radiation (1486.6 eV). The sample was prepared on a stainless-steel holder with conductive double-sided adhesive carbon tape. The electron binding energy was obtained after charge compensation through a flood electron source and was referenced to the C 1s core level at 284.8 eV.

STEM images were acquired using a probe-aberration-corrected JEOL JEM-ARM200F microscope equipped with high-angle annular dark-field, ADF and annular bright-field detectors. For chemical analysis and elemental mapping, the microscope was equipped with a JEOL Dry SD60GV energy-dispersive X-ray spectrometer and a Gatan Enfium ER electron energy-loss spectrometer. EELS elemental maps were calculated from spectrum imaging datasets using the model spectra of the respective elements for pixelwise fitting using Gatan Digital Micrograph 3.5. The catalyst had been dry deposited onto a Cu grid with a holey carbon film.

In situ XAFS spectroscopic measurements were performed at the CAT-ACT beamline of the KIT synchrotron radiation source using a Si (111) double-crystal monochromator<sup>47</sup>. The catalyst powder (1:20 diluted with boron nitride) was loaded into a quartz capillary reactor (diameter, 1.5 mm; wall thickness, 0.02 mm). The measurements were performed at the Fe K edge and the Mn K edge in fluorescence mode. Their conditions are shown in Supplementary Fig. 12. Each catalyst was first heated in 50 vol% H<sub>2</sub>/N<sub>2</sub> (20 ml min<sup>-1</sup>) to 300 °C at a heating rate of 5 °C min<sup>-1</sup> and held at this temperature for 2 h. The reactor was then cooled to 25 °C for the EXAFS measurements. The above-described reduction steps were used for the 10Fe–0Mn, 9Fe–1Mn and 7Fe–3Mn catalysts. After the reduction treatment, the feed (20 ml min<sup>-1</sup>) was changed to CO<sub>2</sub>:H<sub>2</sub>:N<sub>2</sub> = 1:3:6 for the 10Fe–0Mn and 9Fe–1Mn catalysts. The temperature and pressure were increased to 300 °C (at 5 °C min<sup>-1</sup>) and 15 bar, respectively. The catalysts were kept at 300 °C for 2 h and cooled to 25 °C (at 10 °C min<sup>-1</sup>) in the same atmosphere. The same conditions were also used for the reaction at 350 °C for the 9Fe–1Mn catalyst. Normalization of the spectra and EXAFS background subtraction were performed using Athena software<sup>48</sup>. LCA of the XANES spectra was performed in the energy range from –15 eV to +40 eV with respect to the absorption edge. Fourier transformation of the EXAFS oscillations was carried out in the  $k$  range of 3.0–11.5 Å<sup>-1</sup>, and no phase correction was applied.

For the spent catalysts, the ex situ X-ray absorption spectra at the Fe K edge were recorded at the P65 beamline of the PETRA III synchrotron radiation source (DESY) in transmission mode. Samples were analysed in transmission mode as 13 mm pellets pressed with cellulose as a binder. The energy of the X-ray photons was selected using a Si (111) double-crystal monochromator, and the beam size was set using slits measuring 0.3 × 1 mm (vertical × horizontal). The spectra were normalized, and the EXAFS background spectra were subtracted using the Athena program from the IFFEFIT software package<sup>48</sup>. The  $k^2$ -weighted EXAFS functions were Fourier transformed in the  $k$  range of 2–12.3 Å<sup>-1</sup> and multiplied by a Hanning window with a sill size of 1 Å<sup>-1</sup>, and no phase correction was applied.

### Transient kinetic study

The interactions of CO<sub>2</sub> and C<sub>2</sub>H<sub>4</sub> with the promoted or unpromoted catalysts as well as H/D exchange were studied using the TAP-2 reactor. The TAP-2 reactor system, with a resolution of approximately 100 µs, is described in detail elsewhere<sup>49,50</sup>. In the TAP-2 reactor, the reactor exit is physically much closer to the quadrupole mass spectrometer, thus resulting in a substantial enhancement of the detection efficiency

compared with the original TAP-1 system. In a typical experimental procedure, each catalyst (50 mg, 250–350  $\mu\text{m}$  fraction) was loaded between two layers of quartz particles (250–350  $\mu\text{m}$  sieve fraction) in a quartz-tube reactor within its isothermal zone. No catalyst treatment was performed before the experiments. The reactor was evacuated at room temperature to about  $10^{-5}$  Pa and then heated to 300 °C. After this, single-pulse experiments with a  $\text{CO}_2:\text{Ar} = 1:1$ ,  $\text{C}_2\text{H}_4:\text{Ar} = 1:1$  or  $\text{H}_2:\text{D}_2:\text{Ar} = 1:1:1$  mixture were performed at 350 °C. The overall pulse size did not exceed  $\sim 10^{15}$  molecules. Under such conditions, mass transport can be quantitatively described by Knudsen diffusion and any collisions between gas-phase species are minimized. Therefore, only heterogeneous reaction steps were analysed. An on-line quadrupole mass spectrometer (HAL RC 301, Hiden Analytical) was used for analysing gas-phase components leaving the reactor. The following mass-to-charge ( $m/z$ ) values were used for identification of different compounds: 44 ( $\text{CO}_2$ ), 28 ( $\text{CO}$ ,  $\text{CO}_2$ ), 26 ( $\text{C}_2\text{H}_4$ ), 4 ( $\text{D}_2$ ), 3 ( $\text{HD}$ ), 2 ( $\text{H}_2$ ) and 40 ( $\text{Ar}$ ). Pulses were repeated ten times for each  $m/z$  and averaged to improve the signal-to-noise ratio. The concentrations of the feed components and the reaction products were determined from the respective  $m/z$  values using standard fragmentation patterns and sensitivity factors, which arise from the different ionization probabilities of individual compounds. The data evaluation procedure is detailed in the Supplementary Methods.

### Catalytic evaluation

$\text{CO}_2$  hydrogenation tests were carried out using an in-house-developed set-up equipped with 51 fixed-bed stainless-steel tube reactors (outer and inner diameters of 6 and 4 mm, respectively) in parallel. The total feed flow was equally distributed among the reactors. The flow rate passing through each reactor was measured before each experiment. Briefly, the catalyst (0.1 g, 0.25–0.45 mm) was loaded within the reactor isothermal zone. For calculating the segmental rates of  $\text{CO}_2$  conversion and product formation, different catalyst amounts (0.10, 0.05, 0.02, 0.01 and 0.005 g) were used for the  $\text{CO}_2$  hydrogenation tests while the flow rate was kept constant. Descriptions of the segmental rates are given in Supplementary Note 3. Silicon carbide (ESK; 0.7 g, 0.5–0.7 mm) was loaded on top of the catalyst bed to ensure that a plug flow passed through the catalyst bed and to preheat the feed gas. Before the  $\text{CO}_2$ -FTS reaction, the catalyst was reduced in situ at 400 °C and 15 bar in a mixture flow of 50 vol%  $\text{H}_2/\text{N}_2$  (12 ml  $\text{min}^{-1}$ ) for 2 h. After this, the reactors were cooled to the reaction temperature of 250 °C in  $\text{N}_2$ , and the feed mixture ( $\text{CO}_2:\text{H}_2:\text{N}_2 = 1:3:0.3$ ) was introduced.  $\text{N}_2$  was used as the internal standard in gas chromatographic analysis. Reactants and products were evaluated according to the protocols described in the Supplementary Methods.

### Computational methods and models

All calculations were performed using spin-polarized DFT with the projector augmented-wave method<sup>51</sup> as implemented in the Vienna ab initio simulation package<sup>52</sup>. The cut-off energy was set to 400 eV, and the convergence criteria for electronic self-consistent interactions and all forces were set to  $10^{-4}$  eV and 0.05 eV  $\text{\AA}^{-1}$ , respectively. The samplings of the Brillouin zone were generated from the Monkhorst–Pack scheme<sup>53</sup>. For the  $\text{Fe}_5\text{C}_2(510)$  surface, the  $k$ -point mesh generated by the Monkhorst–Pack scheme was chosen to be  $2 \times 2 \times 1$ . The transition states of the elementary steps of  $\text{H}_2$  activation and the hydrogenation of  $\text{C}_2\text{H}_4$  were determined using the climbing image nudged elastic band method<sup>54</sup> and the dimer method<sup>55</sup>, converged to 0.05 eV  $\text{\AA}^{-1}$ , and were further confirmed by vibrational frequency analysis.

The high-Miller-index  $\text{Fe}_5\text{C}_2(510)$  facet is thermodynamically the most stable with the lowest surface Gibbs free energy based on experimental and theoretical studies<sup>56–58</sup>. As the size of the  $\text{Fe}_5\text{C}_2(510)$  slabs was tested and proved to be reasonable in previous studies<sup>59,60</sup>, the same surface model was used in this work, that is, a model system with six Fe layers and five C layers (6Fe/5C), in which the bottom four Fe layers

and three C layers (4Fe/3C) were fixed in their bulk positions, while the top two Fe layers and two C layers (2Fe/2C) were allowed to relax.

According to the core–shell structure and the surface atomic Mn/Fe ratio (−0.45) determined via XPS analysis of the most selective catalyst (9Fe–1Mn; Supplementary Table 1), a model comprising the  $\text{Fe}_5\text{C}_2(510)$  surface with 20 Fe surface atoms covered by a MnO cluster with 10 Mn atoms was created (Supplementary Fig. 44). This surface model results in a MnO monolayer with Mn–O distances ranging from 1.83 to 2.33 Å. Furthermore, the incorporation of a Mn atom into the  $\text{Fe}_5\text{C}_2(510)$  surface structure was considered, and the structure of MnO on the surface is more stable than that obtained by replacing the position of one Fe atom with one Mn atom. The energy of the latter is higher by 0.33 eV, indicating that adsorption of Mn atoms on the  $\text{Fe}_5\text{C}_2(510)$  surface is favoured, consistent with our microscopy observation (Fig. 5).

The adsorption energy ( $\Delta E_{\text{ads}}$ ) of species X is defined as  $\Delta E_{\text{ads}} = E(\text{X}/\text{slab}) - E(\text{slab}) - E(\text{X})$  including the zero-point energy, where  $E(\text{X}/\text{slab})$  is the total energy of the slab model and adsorbent X in equilibrium,  $E(\text{slab})$  is the total energy of the bare slab model and  $E(\text{X})$  is the total energy of free species X in the gas phase. The adsorption enthalpy ( $\Delta H_{\text{ads}}$ ) and adsorption Gibbs free energy ( $\Delta G_{\text{ads}}$ ) are corrected by including the thermal correction to the enthalpy and Gibbs free energy at a given temperature using the VASPKIT program<sup>61</sup>. For discussion and comparison of  $\text{C}_2\text{H}_4$  hydrogenation we used three energy parameters on the reaction coordinates: (1) the Gibbs free energy profile ( $\Delta G$ , including thermal correction to the Gibbs free energy), (2) the enthalpy profile ( $\Delta H$ , including thermal correction to the enthalpy) under the reaction conditions and (3) the energy profile ( $\Delta E$ , including the zero-point energy correction at 0 K). Bader charges for the  $\text{Fe}_5\text{C}_2(510)$  and MnO– $\text{Fe}_5\text{C}_2(510)$  surfaces with the adsorption of a H atom and  $\text{C}_2\text{H}_4$  were calculated as implemented by Henkelman and co-workers<sup>62</sup>.

### Data availability

The data that support the findings of this study are available within the Article and its Supplementary Information. The atomic coordinates of the optimized computational models are provided as Supplementary Data. Source data are provided with this paper.

### References

- Chen, M., Kumar, D., Yi, C.-W. & Goodman, D. W. The promotional effect of gold in catalysis by palladium–gold. *Science* **310**, 291–293 (2005).
- Schlögl, R. Heterogeneous catalysis. *Angew. Chem. Int. Ed.* **54**, 3465–3520 (2015).
- Willis, J. J. et al. Systematic identification of promoters for methane oxidation catalysts using size- and composition-controlled Pd-based bimetallic nanocrystals. *J. Am. Chem. Soc.* **139**, 11989–11997 (2017).
- Huang, X. et al. Atomic-scale observation of the metal–promoter interaction in Rh-based syngas-upgrading catalysts. *Angew. Chem. Int. Ed.* **58**, 8709–8713 (2019).
- Qin, R. et al. Alkali ions secure hydrides for catalytic hydrogenation. *Nat. Catal.* **3**, 703–709 (2020).
- Mortensen, J. J., Hammer, B. & Nørskov, J. K. Alkali promotion of  $\text{N}_2$  dissociation over Ru(0001). *Phys. Rev. Lett.* **80**, 4333–4336 (1998).
- Guo, J. & Chen, P. Ammonia history in the making. *Nat. Catal.* **4**, 734–735 (2021).
- Beck, A. et al. Following the structure of copper–zinc–alumina across the pressure gap in carbon dioxide hydrogenation. *Nat. Catal.* **4**, 488–497 (2021).
- Amann, P. et al. The state of zinc in methanol synthesis over a Zn/ZnO/Cu(211) model catalyst. *Science* **376**, 603–608 (2022).
- Kondratenko, E. V., Mul, G., Baltrusaitis, J., Larrazábal, G. O. & Pérez-Ramírez, J. Status and perspectives of  $\text{CO}_2$  conversion into fuels and chemicals by catalytic, photocatalytic and electrocatalytic processes. *Energy Environ. Sci.* **6**, 3112–3135 (2013).

11. Ye, R.-P. et al. CO<sub>2</sub> hydrogenation to high-value products via heterogeneous catalysis. *Nat. Commun.* **10**, 5698 (2019).
12. Wei, J., Yao, R., Han, Y., Ge, Q. & Sun, J. Towards the development of the emerging process of CO<sub>2</sub> heterogenous hydrogenation into high-value unsaturated heavy hydrocarbons. *Chem. Soc. Rev.* **50**, 10764–10805 (2021).
13. Wei, J. et al. Directly converting CO<sub>2</sub> into a gasoline fuel. *Nat. Commun.* **8**, 15174 (2017).
14. Ramirez, A. et al. Selectivity descriptors for the direct hydrogenation of CO<sub>2</sub> to hydrocarbons during zeolite-mediated bifunctional catalysis. *Nat. Commun.* **12**, 5914 (2021).
15. Zhu, J. et al. Dynamic structural evolution of iron catalysts involving competitive oxidation and carburization during CO<sub>2</sub> hydrogenation. *Sci. Adv.* **8**, eabm3629 (2022).
16. Guo, L. et al. High-yield production of liquid fuels in CO<sub>2</sub> hydrogenation on a zeolite-free Fe-based catalyst. *Chem. Sci.* **14**, 171–178 (2023).
17. Aitbekova, A. et al. Engineering of ruthenium–iron oxide colloidal heterostructures: improved yields in CO<sub>2</sub> hydrogenation to hydrocarbons. *Angew. Chem. Int. Ed.* **58**, 17451–17457 (2019).
18. Yao, B. et al. Transforming carbon dioxide into jet fuel using an organic combustion-synthesized Fe–Mn–K catalyst. *Nat. Commun.* **11**, 6395 (2020).
19. Yang, S. et al. Comparative study of olefin production from CO and CO<sub>2</sub> using Na- and K-promoted zinc ferrite. *ACS Catal.* **10**, 10742–10759 (2020).
20. Zhang, C. et al. Unraveling the role of zinc on bimetallic Fe<sub>3</sub>C<sub>2</sub>–ZnO catalysts for highly selective carbon dioxide hydrogenation to high carbon  $\alpha$ -olefins. *ACS Catal.* **11**, 2121–2133 (2021).
21. Li, Z. et al. Ambient-pressure hydrogenation of CO<sub>2</sub> into long-chain olefins. *Nat. Commun.* **13**, 2396 (2022).
22. Barrios, A. J. et al. Efficient promoters and reaction paths in the CO<sub>2</sub> hydrogenation to light olefins over zirconia-supported iron catalysts. *ACS Catal.* **12**, 3211–3225 (2022).
23. Al-Dossary, M., Ismail, A. A., Fierro, J. L. G., Bouzid, H. & Al-Sayari, S. A. Effect of Mn loading onto MnFeO nanocomposites for the CO<sub>2</sub> hydrogenation reaction. *Appl. Catal. B* **165**, 651–660 (2015).
24. Xu, Y. et al. Highly selective olefin production from CO<sub>2</sub> hydrogenation on iron catalysts: a subtle synergy between manganese and sodium additives. *Angew. Chem. Int. Ed.* **59**, 21736–21744 (2020).
25. Li, Y. et al. Direct conversion of carbon dioxide into liquid fuels and chemicals by coupling green hydrogen at high temperature. *Appl. Catal. B* **324**, 122299 (2023).
26. Maiti, G. C., Malessa, R. & Baerns, M. Iron/manganese oxide catalysts for Fischer–Tropsch synthesis. Part I: structural and textural changes by calcination, reduction and synthesis. *Appl. Catal.* **5**, 151–170 (1983).
27. Maiti, G. C., Malessa, R., Löchner, U., Papp, H. & Baerns, M. Iron/manganese oxide catalysts for Fischer–Tropsch synthesis. Part II: crystal phase composition, activity and selectivity. *Appl. Catal.* **16**, 215–225 (1985).
28. Dinse, A., Aigner, M., Ulbrich, M., Johnson, G. R. & Bell, A. T. Effects of Mn promotion on the activity and selectivity of Co/SiO<sub>2</sub> for Fischer–Tropsch synthesis. *J. Catal.* **288**, 104–114 (2012).
29. Xie, J. et al. Promoted cobalt metal catalysts suitable for the production of lower olefins from natural gas. *Nat. Commun.* **10**, 167 (2019).
30. Ding, X., Zhu, M., Han, Y.-f & Yang, Z. Revisiting the syngas conversion to olefins over Fe–Mn bimetallic catalysts: insights from the proximity effects. *J. Catal.* **417**, 213–225 (2023).
31. Xu, Y. et al. A hydrophobic FeMn@Si catalyst increases olefins from syngas by suppressing C1 by-products. *Science* **371**, 610–613 (2021).
32. Zhang, P. et al. Controllable assembly of Fe<sub>3</sub>O<sub>4</sub>–Fe<sub>3</sub>C@MC by in situ doping of Mn for CO<sub>2</sub> selective hydrogenation to light olefins. *Catal. Sci. Technol.* **12**, 2360–2368 (2022).
33. Liu, B. et al. Unravelling the new roles of Na and Mn promoter in CO<sub>2</sub> hydrogenation over Fe<sub>3</sub>O<sub>4</sub>-based catalysts for enhanced selectivity to light  $\alpha$ -olefins. *ChemCatChem* **10**, 4718–4732 (2018).
34. van Dijk, W. L., Niemantsverdriet, J. W., van der Kraan, A. M. & van der Baan, H. S. Effects of manganese oxide and sulphate on the olefin selectivity of iron catalysts in the Fischer Tropsch reaction. *Appl. Catal.* **2**, 273–288 (1982).
35. Yang, H. et al. Selective synthesis of olefins via CO<sub>2</sub> hydrogenation over transition-metal-doped iron-based catalysts. *Appl. Catal. B* **321**, 122050 (2023).
36. Maurer, F. et al. Tracking the formation, fate and consequence for catalytic activity of Pt single sites on CeO<sub>2</sub>. *Nat. Catal.* **3**, 824–833 (2020).
37. Muravev, V. et al. Interface dynamics of Pd–CeO<sub>2</sub> single-atom catalysts during CO oxidation. *Nat. Catal.* **4**, 469–478 (2021).
38. Chen, L. et al. Dynamic evolution of palladium single atoms on anatase titania support determines the reverse water–gas shift activity. *J. Am. Chem. Soc.* **145**, 10847–10860 (2023).
39. Monai, M. et al. Restructuring of titanium oxide overlayers over nickel nanoparticles during catalysis. *Science* **380**, 644–651 (2023).
40. Arinchtin, A. et al. Dynamics of reaction-induced changes of model-type iron oxide phases in the CO<sub>2</sub>-Fischer–Tropsch-synthesis. *ChemCatChem* **14**, e202200240 (2022).
41. Ding, X., Zhu, M., Sun, B., Yang, Z. & Han, Y.-F. An overview on dynamic phase transformation and surface reconstruction of iron catalysts for catalytic hydrogenation of CO<sub>x</sub> for hydrocarbons. *ACS Catal.* **14**, 6137–6168 (2024).
42. Yang, Q. et al. Identifying performance descriptors in CO<sub>2</sub> hydrogenation over iron-based catalysts promoted with alkali metals. *Angew. Chem. Int. Ed.* **61**, e202116517 (2022).
43. Yang, Q. et al. Activity and selectivity descriptors for iron carbides in CO<sub>2</sub> hydrogenation. *Appl. Catal. B* **327**, 122450 (2023).
44. Skrypnik, A. S. et al. Descriptors affecting methane selectivity in CO<sub>2</sub> hydrogenation over unpromoted bulk iron(III)-based catalysts. *ACS Catal.* **12**, 11355–11368 (2022).
45. Darken, L. S. & Gurry, R. W. The system iron–oxygen. I. The wüstite field and related equilibria. *J. Am. Chem. Soc.* **67**, 1398–1412 (1945).
46. Jin, Y., Xu, H. & Datye, A. K. Electron energy loss spectroscopy (EELS) of iron Fischer–Tropsch catalysts. *Microsc. Microanal.* **12**, 124–134 (2006).
47. Zimina, A. et al. CAT-ACT—a new highly versatile X-ray spectroscopy beamline for catalysis and radionuclide science at the KIT synchrotron light facility ANKA. *Rev. Sci. Instrum.* **88**, 113113 (2017).
48. Ravel, B. & Newville, M. ATHENA, ARTEMIS, HEPHAESTUS: data analysis for X-ray absorption spectroscopy using IFEFFIT. *J. Synchrotron Radiat.* **12**, 537–541 (2005).
49. Gleaves, J. T., Yablonskii, G. S., Phanawadee, P. & Schuurman, Y. TAP-2: an interrogative kinetics approach. *Appl. Catal. A* **160**, 55–88 (1997).
50. Pérez-Ramírez, J. & Kondratenko, E. V. Evolution, achievements, and perspectives of the TAP technique. *Catal. Today* **121**, 160–169 (2007).
51. Blöchl, P. E. Projector augmented-wave method. *Phys. Rev. B* **50**, 17953–17979 (1994).
52. Kresse, G. Ab initio molecular dynamics for liquid metals. *J. Non Cryst. Solids* **192–193**, 222–229 (1995).
53. Monkhorst, H. J. & Pack, J. D. Special points for Brillouin-zone integrations. *Phys. Rev. B* **13**, 5188–5192 (1976).
54. Henkelman, G., Uberuaga, B. P. & Jónsson, H. A climbing image nudged elastic band method for finding saddle points and minimum energy paths. *J. Chem. Phys.* **113**, 9901–9904 (2000).



55. Henkelman, G. & Jónsson, H. A dimer method for finding saddle points on high dimensional potential surfaces using only first derivatives. *J. Chem. Phys.* **111**, 7010–7022 (1999).
56. Pham, T. H., Duan, X., Qian, G., Zhou, X. & Chen, D. CO activation pathways of Fischer–Tropsch synthesis on  $\chi$ -Fe<sub>3</sub>C<sub>2</sub>(510): direct versus hydrogen-assisted CO dissociation. *J. Phys. Chem. C* **118**, 10170–10176 (2014).
57. Liu, Q.-Y., Shang, C. & Liu, Z.-P. In situ active site for CO activation in Fe-catalyzed Fischer–Tropsch synthesis from machine learning. *J. Am. Chem. Soc.* **143**, 11109–11120 (2021).
58. Yang, C., Zhao, H., Hou, Y. & Ma, D. Fe<sub>3</sub>C<sub>2</sub> nanoparticles: a facile bromide-induced synthesis and as an active phase for Fischer–Tropsch synthesis. *J. Am. Chem. Soc.* **134**, 15814–15821 (2012).
59. Zhao, S. et al. Surface morphology of Hägg iron carbide ( $\chi$ -Fe<sub>3</sub>C<sub>2</sub>) from ab initio atomistic thermodynamics. *J. Catal.* **294**, 47–53 (2012).
60. He, Y. et al. Hunting the correlation between Fe<sub>3</sub>C<sub>2</sub> surfaces and their activities on CO: the descriptor of bond valence. *J. Phys. Chem. C* **122**, 2806–2814 (2018).
61. Wang, V., Xu, N., Liu, J.-C., Tang, G. & Geng, W.-T. VASPKIT: a user-friendly interface facilitating high-throughput computing and analysis using VASP code. *Comput. Phys. Commun.* **267**, 108033 (2021).
62. Henkelman, G., Arnaldsson, A. & Jónsson, H. A fast and robust algorithm for Bader decomposition of charge density. *Comput. Mater. Sci.* **36**, 354–360 (2006).

## Acknowledgements

This work was funded by the Deutsche Forschungsgemeinschaft (DFG) under the priority program SPP 2080 (grant nos. KO 2261/10-1 and KO 2261/10-2 (E.V.K.), BR 1380/29-1 and BR 1380/29-2 (A.B.) and GR 3987/13-2 and GR 3987/14-2 (J.-D.G.)). D.-B.C. is grateful for financial support from the National Natural Science Foundation of China (no. 22372186). Q.Y. thanks R. Eckelt and A. Simmla for performing the N<sub>2</sub> adsorption–desorption experiments and ICP-OES measurements, respectively. We acknowledge the CAT-ACT beamline at the KIT synchrotron facility (KARA) for providing access to synchrotron radiation, and A. Zimina for the technical support during the in situ XAS measurements. Part of the XAS experiments were carried out at PETRA III of DESY (Hamburg, Germany), a member of the Helmholtz Association HGF, and we would like to thank M. Desmau and E. Welter for their assistance in using beamline P65 (proposal I-20210242) and infrastructure by ErUM-Pro (BMBF). We thank the German Federal Ministry for Education and Research (BMBF) for funding the EELS spectrometer in the frame of project ESMAC.

## Author contributions

E.V.K. and Q.Y. conceived the research. Q.Y. prepared the catalysts and performed the general characterization and reaction tests. E.A.F., E.S., D.E.D., J.-D.G., A.B. and Q.Y. contributed to the measurement,

analysis and discussion of the in situ/ex situ XAS data. D.-B.C. and H.J. performed the the DFT study and prepared the draft of the DFT part. V.A.K. conducted the TAP experiments and analysed the results. C.R.K. performed the TEM analyses. H.L. performed the XRD measurements and quantitative analysis. S.B. collected and analysed the XPS data. J.W., E.A.F. and A.B. performed the Raman experiments. Q.Y. and E.V.K. wrote the first draft of this article with the input from all other co-authors.

## Funding

Open access funding provided by Leibniz-Institut für Katalyse e.V. (LIKAT Rostock).

## Competing interests

The authors declare no competing interests.

## Additional information

**Supplementary information** The online version contains supplementary material available at <https://doi.org/10.1038/s41929-025-01334-5>.

**Correspondence and requests for materials** should be addressed to Qingxin Yang or Evgenii V. Kondratenko.

**Peer review information** *Nature Catalysis* thanks Evgeniy Redekop and the other, anonymous, reviewer(s) for their contribution to the peer review of this work.

**Reprints and permissions information** is available at [www.nature.com/reprints](http://www.nature.com/reprints).

**Publisher's note** Springer Nature remains neutral with regard to jurisdictional claims in published maps and institutional affiliations.

**Open Access** This article is licensed under a Creative Commons Attribution 4.0 International License, which permits use, sharing, adaptation, distribution and reproduction in any medium or format, as long as you give appropriate credit to the original author(s) and the source, provide a link to the Creative Commons licence, and indicate if changes were made. The images or other third party material in this article are included in the article's Creative Commons licence, unless indicated otherwise in a credit line to the material. If material is not included in the article's Creative Commons licence and your intended use is not permitted by statutory regulation or exceeds the permitted use, you will need to obtain permission directly from the copyright holder. To view a copy of this licence, visit <http://creativecommons.org/licenses/by/4.0/>.

© The Author(s) 2025